A NEW FLYBACK DC-TO-THREE-PHASE CONVERTER WITH SINUSOIDAL OUTPUTS

KHAI D. T. NGO, SLOBODAN ĆUK, AND R.D. MIDDLEBROOK

Power Electronics Group
California Institute of Technology

ABSTRACT

Systematic extension of any dc-to-dc converter leads to its dc-to-three-phase equivalent characterized by sinusoidal output voltages and fast dynamic responses. This generalization principle is illustrated for the special case of the flyback topology. State-space averaging has modeled with a high degree of accuracy the performance of dc-to-dc converters. Here it is combined with the stationary-to-rotating coordinate transformation, customarily used in polyphase ac systems, to result in an effective analysis method for switched-mode dc-to-polyphase converters.

1. INTRODUCTION

A variety of switched-mode topologies have been used to invert a dc input into three-phase outputs for such applications as ac motor drives. Well-known inverters at the low switching frequency end are the Voltage-Source and Current-Source inverters and their modifications [1]. These circuits switch at the inversion frequency, and their outputs consequently are six-stepped *square waves* of voltage or current. This kind of waveshape inevitably induces harmonic heating and low-frequency torque pulsation in ac machines. Since amplitude variation is usually exercised through the dc link via phase-control, harmonics are sent back into the line. The expensive, bulky inductor embedded in the current-source inverter often limits the response speed and operating frequency range.

This work was supported in part by the Office of Naval Research, Washington DC, under Contract N00014-78-C-0757 and by the Naval Ocean Systems Center, San Diego, CA.

Recently a group of Polyphase Switching Power Amplifiers [2] has emerged as an example of high-frequency switched-mode inversion. Since these amplifiers are constructed from dc-to-dc building blocks, their open-loop phase voltages generally inherit distorted sinusoids riding on high dc offsets. They can thus be categorized as *descendents* of dc-to-dc converters. Yet to be uncovered is the *equivalence* to the family of dc-to-dc topologies: the class of dc-to-polyphase converters.

The motivation is thus clear: *to search for a compact open-loop configuration capable of generating truly sinusoidal balanced three-phase outputs from a dc source and easy-to-synthesize switching functions.*

Section 2 repeats the historical development that originates the flyback dc-to-three-phase converter. The state-space averaged description of the system in the stationary *abc* reference frame is written at the beginning of Section 3 and then solved to confirm the ideal steady-state waveshapes. Section 4 transforms the dynamic equations to the rotating *αβ* axes and discusses the ac small-signal transfer functions of the converter in this frame. The practical implementation of the new topology is delineated in Section 5; it is then used to confirm earlier theoretical predictions. Section 6 summarizes the salient features of the analysis.

2. DESCRIPTION OF THE FLYBACK DC-TO-THREE-PHASE TOPOLOGY

The flyback dc-to-three-phase converter results from a systematic generalization of its dc-to-dc kin. The development procedure for this particular topology is explained in this section with the hope that it helps to visualize the synthesis of the remaining converters (buck, boost, etc.) of the family. A good way to start is to review the essential features of the familiar flyback dc-to-dc circuit.

0275-9306/83/0000-0377 $1.00

2.1 Review of the Flyback Dc-to-Dc-Topology

Figure 1a sketches a more general version of the familiar flyback dc-to-dc converter. The inductor communicates with the rest of the circuit through two single-pole, double-throw switches. Each throw can be characterized by its own *switching function* as assigned in Fig. 1b. The time average of a switching function d(t) is called the *duty ratio* $\langle d(t) \rangle$, where brackets symbolize an averaged quantity.

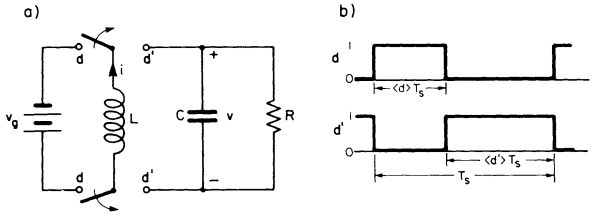

Fig. 1. (a) Flyback dc-to-dc converter and (b) its switching functions.

Figure 1b defines two distinct switching topologies for the circuit in Fig. 1a. During $\langle d \rangle T_s$ the inductor is connected across v_g and gets charged while the capacitor supports the load. The energy in the inductor is then dumped into the RC combination during $\langle d' \rangle T_s$. Both state-space averaging [3] and the volt-second-balance principle predict the steady-state output voltage to be

$$V = \frac{D}{D'} V_g \qquad (1)$$

where

$D \equiv$ steady-state $\langle d \rangle$, and $D' = 1 - D$

Ac operation can be extracted from the topology in Fig. 1a by large-signally modulating $\langle d \rangle$ and $\langle d' \rangle$. Unfortunately, high-quality three-phase voltages cannot be obtained simply by putting three sinusoidally-modulated dc converters together because the nonlinearity in (1) always induces distortion at the outputs. It is thus desirable to introduce a new flyback dc-to-three-phase topology that inherently generates *clean* polyphase power.

2.2 Flyback Dc-to-Three-Phase Topology

The sequence of energy storage and transfer in the dc-to-dc circuit can be used as the constructing principle for a three-phase converter, and the new topology may conceivably have only one inductor that is applied across v_g during $\langle d \rangle T_s$ and then is sequentially connected to the three outputs during $\langle d' \rangle T_s$. Therefore, the arrangement of v_g with L at the input end should be adopted without further modification from the input section of Fig. 1a. The only difference in going from single-phase to three-phase lies in the output part: there are now three, instead of one, outputs, and so it is logical to add two extra capacitors to make two more outputs.

Two new outputs necessarily require two more throws in each switch. Hence, the inductor now transfers energy through two single-pole, quadruple-throw switches, as pictured in Fig. 2a. Note that two identical throws on the v_g side can be merged into one, and so only seven generally distinct switching functions (Fig. 2b) are necessary to characterize the converter. The extension of Fig. 2a to *more than three phases* is obvious.

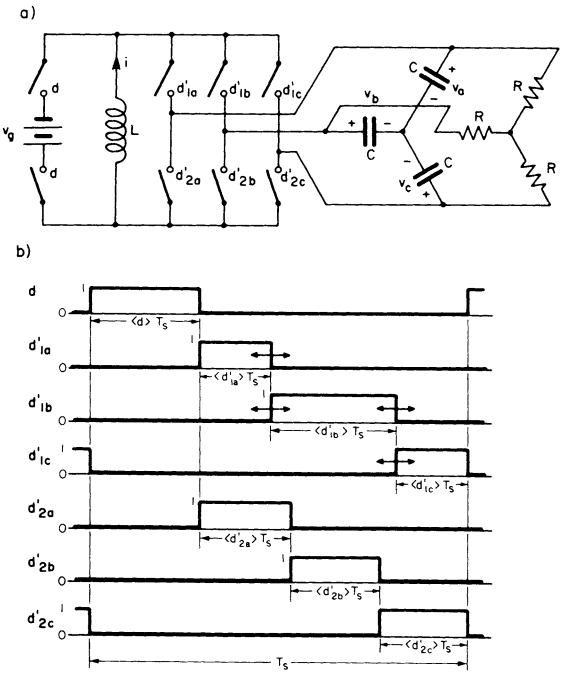

Fig. 2. (a) Flyback dc-to-three-phase converter with one inductor and three capacitors and (b) its switching functions.

Regardless of the exact nature of the duty ratios, the topology in Fig. 2a functions similarly to that in Fig. 1a. The inductor is connected across v_g during $\langle d \rangle T_s$ and across the output for the remainder of the cycle. In their most versatile forms, the two switches act completely *independently* of each other during $\langle d' \rangle T_s$. This flexibility leads to a *variety* of useful switching strategies that all produce sinusoidal outputs.

One obvious feature of the new converter is that it allows *isolation*, merely by splitting the inductor into two coupled windings.

The important unanswered question at this point is: what *simple duty ratios* must be synthesized into the switching functions of Fig. 2b so that the open-loop topology of Fig. 2a indeed produces *zero-averaged sinusoidal* voltages. To resolve this question and to understand the converter more require the averaged state-space description of the system.

2.3 The "abc" State-Space Averaged Equations

The following analysis assumes ideal conditions, such as balanced three-phase components, perfect switches, sufficiently fast switching frequencies, etc. Among the fundamental approximations of state-space averaging [3] that must be strictly observed is the small, linear ripple assumption. Furthermore, the highest frequency component in any duty ratio should be well below half the switching frequency for the prediction to be valid.

It is convenient to introduce a refined, systematic approach to obtain the averaged state-space equations for a *complex multiple-pole, multiple-throw* (MPMT) *switching structure* such as that in Fig. 2a. This method realizes a fundamental modeling difficulty rarely encountered in two-topology switching networks, namely, both the *number* and the *type* of switching topologies in MPMT switching converters may *vary from cycle to cycle* if at least one duty ratio is time-varying. Fortunately, first-order approximations in the state-space averaging process are insensitive to these variations, and it is possible to show that all switching cycles can be characterized by a *unique* set of state-space averaged equations. These equations, in turn, can be expediently obtained by replacing each *switching function* in the *exact time-domain state-space equations* by its corresponding *duty ratio*. For instance, if the capacitor common is chosen as the reference during $\langle d' \rangle T_s$, then the *exact* dynamic equation for the inductor is

$$L\frac{di}{dt} = dv_g + (d'_{2a}v_a + d'_{2b}v_b + d'_{2c}v_c) - (d'_{1a}v_a + d'_{1b}v_b + d'_{1c}v_c) \qquad (2)$$

The first term on the right-hand side of (2) represents the application of v_g to L during $\langle d \rangle T_s$; the second and third terms describe the waveforms at the positive and negative ends, respectively, of the inductor during $\langle d' \rangle T_s$. The *state-space averaged* equation for L can now be constructed by substitution of $\langle d \rangle$ for d, $\langle d'_{1a} \rangle$ for d'_{1a}, etc., in (2):

$$L\frac{di}{dt} = -(\langle d'_{1a}\rangle - \langle d'_{2a}\rangle)v_a - (\langle d'_{1b}\rangle - \langle d'_{2b}\rangle)v_b - (\langle d'_{1c}\rangle - \langle d'_{2c}\rangle)v_c + \langle d \rangle v_g \qquad (3)$$

Dynamic equations for the capacitors can be derived in a similar fashion. Since each pair $\langle d'_{1\alpha} \rangle$ and $\langle d'_{2\alpha} \rangle$ ($\alpha \equiv a,b,c$) always appear together as $\langle d'_{1\alpha}\rangle - \langle d'_{2\alpha}\rangle$), it is convenient to define

$$d'_\alpha = \langle d'_{1\alpha} \rangle - \langle d'_{2\alpha} \rangle \text{ for } \alpha \equiv a,b,c \qquad (4)$$

The capacitor equations can now be grouped with (3) to form the system matrix equation

$$P\frac{dx}{dt} = A\,x + B\,u \qquad (5a)$$

where

$$x = [i \;\; v_a \;\; v_b \;\; v_c]^T, \quad u = v_g \qquad (5b,c)$$

$$A = \begin{bmatrix} 0 & -d'_a & -d'_b & -d'_c \\ d'_a & -2/3R & 1/3R & 1/3R \\ d'_b & 1/3R & -2/3R & 1/3R \\ d'_c & 1/3R & 1/3R & -2/3R \end{bmatrix} \qquad (5d)$$

$$B = \begin{bmatrix} \langle d \rangle \\ 0 \\ 0 \\ 0 \end{bmatrix}, \text{ and } \quad P = \begin{bmatrix} L & 0 & 0 & 0 \\ 0 & C & 0 & 0 \\ 0 & 0 & C & 0 \\ 0 & 0 & 0 & C \end{bmatrix} \qquad (5e,f)$$

The inductor contributes the first term on the right-hand side of each capacitor equation, and the load gives rise to the remaining terms. Equations (5) are called the "abc" state-space averaged equations because they are derived in the usual stationary time coordinate that characterizes three balanced three-phase quantities as *a*, *b*, and *c* components.

Nothing has been said so far about the exact nature of the duty ratios $\langle d \rangle$ and $\langle d'_{i\alpha} \rangle$ ($i = 1,2$ and $\alpha \equiv a,b,c$). It is desirable that they contain only *simple* functions like *dc* or *sinusoids*. They also ought to be *positive* to be realizable. An obvious choice of $\langle d'_{i\alpha} \rangle$ that satisfies these criteria is

$$\langle d'_{1a} \rangle = \frac{\langle d' \rangle}{3} + \frac{d'_m}{3}\cos\theta \qquad (6a)$$

$$\langle d'_{1b} \rangle = \frac{\langle d' \rangle}{3} + \frac{d'_m}{3}\cos(\theta - 120^0) \qquad (6b)$$

$$\langle d'_{1c} \rangle = \frac{\langle d' \rangle}{3} + \frac{d'_m}{3}\cos(\theta + 120^0) \qquad (6c)$$

and

$$\langle d'_{2a} \rangle = \langle d'_{2b} \rangle = \langle d'_{2c} \rangle = \frac{\langle d' \rangle}{3} \qquad (6d)$$

where

$$\langle d' \rangle = 1 - \langle d \rangle, \quad d'_m \le \langle d' \rangle, \quad \theta = \int_0^t \omega(\tau)\,d\tau \qquad (6e,f,g)$$

In the above, d'_m and ω are instantaneous modulation amplitude and frequency, respectively. In general, $\langle d'_{2\alpha} \rangle$ can contain ac modulation whose amplitude and phase *differ* from those of $\langle d'_{1\alpha} \rangle$. However, as a special case, the ac component of $\langle d'_{2\alpha} \rangle$ is set to zero by virtue of (6d).

Equations (6a) through (6d) can be used in (4) to compute d'_α:

$$d'_a = \frac{d'_m}{3}\cos\theta \qquad (7)$$

and so on for d_b' and d_c'. Equations (4) through (7) completely characterize the steady-state and dynamic behaviors of the flyback dc-to-three-phase converter. The steady-state results will be discussed first in the following section.

3. STEADY-STATE ANALYSIS

3.1 Steady-State Solutions

The control inputs to the converter can easily be identified as $\langle d \rangle$, d_m', ω, and v_g from (5) and (7). Under steady-state condition, they consist of only dc components correspondingly denoted as D, D_m', Ω, and V_g. The next step is to solve (5) that is already *nonlinear* due to the products $d_\alpha' v_\alpha$ and $d_\alpha' i$. Since the original objective asserts that the proposed topology is worthy only when its outputs are purely sinusoidal, the capacitor voltages can only be

$$v_a = V_{os} + V \cos(\Omega t - \Phi_v) \tag{8}$$

where capital letters imply dc steady states, and so on for v_b and v_c. Observe that the expected solutions include a dc offset component V_{os} that may exist and yet affects neither the inductor nor the load. With the voltages constituting a balanced three-phase set as described in (8), the instantaneous output and, hence, input powers are constant. Since D and V_g are already dc, constant instantaneous input power implies *dc* inductor current, i.e.,

$$i \equiv I \tag{9}$$

during steady state.

It remains to substitute (8) and (9) into (5) and solve for I, V, Φ_v, and V_{os}. After straightforward algebraic manipulation, the results are

$$I = 6 \frac{DV_g}{D_m'^2 R} \left[1 + \left(\frac{\Omega}{\omega_p} \right)^2 \right] \tag{10a}$$

$$V e^{-j\Phi_v} = 2 \frac{DV_g}{D_m'} \left(1 - \frac{j\Omega}{\omega_p} \right) \tag{10b}$$

and

$$V_{os} \equiv \textit{indeterminate} \tag{10c}$$

where

$$\omega_p = \frac{1}{RC} \tag{10d}$$

The current in (10a) and the voltage in (10b) obviously satisfy the conservation-of-power requirement. Note that phasor notation is used in (10b) to establish a consistency in symbolizing steady-state solutions: all these quantities are now characterized by constants. Under this convention, a *real constant* (Eq.(10a)) represents *dc steady state* while a *complex constant* (Eq. (10b)) indicates *sinusoidal steady state*.

3.2 Comments on Steady-State Solutions

Equation (10a) confirms the assumption that the *inductor current is dc*. Most eminent is the dependence of I on Ω^2 that ultimately imposes a power restriction on high-frequency operation. To understand why the current increases at such a fast rate requires a look at the voltage behavior.

The very existence of (10b) proves that the new topology indeed generates *clean sinusoidal three-phase voltages*. Closer investigation of this equation, however, reveals an unexpected, interesting phenomenon: the steady-state voltage phasor possesses a "*right half-plane (rhp) zero*" in its frequency dependence. To be more descriptive, the voltage amplitude keeps on increasing while the phase (referenced to d_a') continues lagging as the modulation frequency is swept upward. Although this odd behavior defies intuition, it can be explained in simple words once the phase variation is separated from the voltage trend.

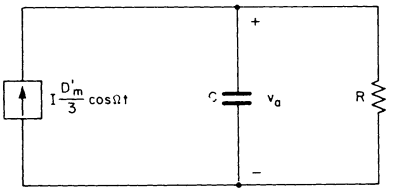

Fig. 3. Virtual parallel connection of R and C fed by the inductor current to explain the steady-state phase lag.

Figure 3 accounts for the phase change by modeling the inductor as a frequency-dependent current source (Eq. (5)) feeding into the virtually parallel RC combination of phase *a* (Fig. 2a). Linear circuit theory can be used to show that v_a always lags d_a' by $\tan^{-1}(\Omega/\omega_p)$, the same as the angle given in (10b). Once the phase change has been established, the amplitude rise can be explained by interpreting the volt-second-balance criteria in (5). The output voltages supply volt-seconds through the sum $(d_a' v_a + d_b' v_b + d_c' v_c)$ that is proportional to $V \cos\Phi_v$. As the output waveform "slips" away from the duty ratio with increasing frequency, $\cos\Phi_v$ *decreases* to reflect the less efficient contribution from the voltages. The amplitude V then has to *increase* to compensate for this loss, and hence the "rhp zero."

Apart from the frequency dependence, the amplitude of (10b) looks similar to that of (1). The "effective D'" is $D_m'/2$, the factor 1/2 resulting from the particular assignment of duty ratios in (6). The dc-to-three-phase converter thus can step the input both up and down. Control of the output amplitude can easily be achieved at the signal level through D and D_m' although it can be less efficiently done at the power level via V_g.

Leakage across real-life capacitors cures the arbitrariness of V_{os} (Eq. (10c)) by fixing this dc offset to zero; so practical converters indeed have *zero-averaged, sinusoidal* outputs. The oncoming dynamic analysis effectively ignores v_{os} because this voltage does not participate in the power inversion process.

4. DYNAMIC ANALYSIS

4.1 The "$o\mathcal{G}b$" Transformation

As was demonstrated, state-space averaging modeled a switching network by combining all sets of linear, time-invariant differential equations describing the various switching topologies into a unique set of linear, time-variant differential equations characterizing an equivalent continuous circuit. In dc-to-dc converters the small-signal analysis then follows by perturbing the dc control variables embedded in the system equations. Such an approach, however, does not extend directly to the case of dc-to-three-phase inverters because many steady-state quantities in these networks are already sinusoidally *time-varying*. Fortunately, a variety of analytical tools are available in the literature to treat the dynamics of polyphase machines, and they can be readily borrowed for the small-signal study of the polyphase topology being presented.

The aforementioned methods center around the choice of a suitable frame of reference in which the state-space averaged equations exhibit *time-invariant steady-state* behavior. Many such frames exist for the topology being studied owing to its ideal waveshapes. The one chosen for this paper is the "$o\mathcal{G}b$" reference frame, and the corresponding transformation that converts balanced three-phase sinusoids to complex constants is named the "$o\mathcal{G}b$" transformation [4].

This transformation is based on the principle that the *rotating sum* of polyphase space phasors properly displaced in time phase appears *stationary* in a *coordinate rotating at the same instantaneous velocity*. Let the *abc* voltage vector, the $o\mathcal{G}b$ voltage vector, and the $o\mathcal{G}b$ transformation be respectively defined as

$$\underline{v} = [v_a \; v_b \; v_c]^T, \quad \underline{\nu} = [v_o \; \nu_f \; \nu_b]^T \tag{11a,b}$$

and

$$T_v = \frac{1}{\sqrt{3}} \begin{bmatrix} 1 & e^{-j\theta_T} & e^{j\theta_T} \\ 1 & e^{-j(\theta_T-120^0)} & e^{j(\theta_T-120^0)} \\ 1 & e^{-j(\theta_T+120^0)} & e^{j(\theta_T+120^0)} \end{bmatrix} \tag{11c}$$

where

$$\theta_T = \int_0^t \omega(\tau)d\tau - \Phi_T \tag{11d}$$

and script denotes complex variables. Then if $\Phi_T = 0$, the operation

$$\underline{v} = T_v \, \underline{\nu} \tag{12}$$

transforms $\underline{v}$, whose steady-state components are given in (8), into

$$\underline{\nu} = \left[\sqrt{3}\, v_{os} \quad \frac{\sqrt{3}}{2} v\, e^{j\phi_v} \quad \frac{\sqrt{3}}{2} v\, e^{-j\phi_v}\right]^T \tag{13}$$

So v_o, the "zero-sequence component," reflects the dc offset while ν_b, the "backward component," characterizes the voltage phasor. The "forward component" ν_f is actually redundant but is nevertheless carried along to maintain mathematical symmetry.

The transformed variables clearly eliminate all time dependence. Interest can now be directed toward deriving the *transformed state-space averaged equations*.

4.2 The "$o\mathcal{G}b$" State-Space Averaged Equations

Under the transformation

$$\underline{x} = T \, \underline{x} \tag{14}$$

where

$$\underline{x} = [i \; v_o \; \nu_f \; \nu_b]^T, \quad T = \begin{bmatrix} 1 & \underline{0}^T \\ \underline{0} & T_v \end{bmatrix} \tag{15a,b}$$

where

$$T_v = (11c) \text{ with } \Phi_T = 0$$

(5) becomes

$$P \frac{d\underline{x}}{dt} = A \, \underline{x} + B \, \underline{u} \tag{16a}$$

where

$$A = \begin{bmatrix} 0 & 0 & -d_m'/2\sqrt{3} & -d_m'/2\sqrt{3} \\ 0 & 0 & 0 & 0 \\ d_m'/2\sqrt{3} & 0 & -1/R + j\omega C & 0 \\ d_m'/2\sqrt{3} & 0 & 0 & -1/R - j\omega C \end{bmatrix} \tag{16b}$$

and $\underline{x}$, $\underline{u}$, B, and P are as defined in (15a) and (5). Note that the $o\mathcal{G}b$ transformation is invoked only once to act upon the sinusoidal voltages. The inductor current, being dc, is passed straight to the new frame.

In the rotating $o\mathcal{G}b$ coordinate, the system description (Eq. (16)) consists of a set of *nonlinear* inhomogeneous differential equations with *constant complex coefficients*. The zero second row and column in the A matrix decouple v_o from the other states and confirm the indeterminacy of this component, and so v_o and its corresponding rows and columns in (16) can be deleted to bring the order of the system from four down to three. Further rearrangement then culminates in the following more illuminating format:

$$P'\frac{d\underline{x}'}{dt} = (A_R + d'_{me}A_{d'} + j\omega A_\omega)\,\underline{x}' + \langle d\rangle B_d v_g \quad (17a)$$

where

$$d'_{me} = \frac{d'_m}{2\sqrt{3}}, \quad \underline{x}' = [i\ v_f\ v_b]^T, \quad B_d = [1\ 0\ 0]^T \quad (17b,c,d)$$

$$A_{d'} = \begin{bmatrix} 0 & -1 & -1 \\ 1 & 0 & 0 \\ 1 & 0 & 0 \end{bmatrix}, \quad A_R = \begin{bmatrix} 0 & 0 & 0 \\ 0 & -1/R & 0 \\ 0 & 0 & -1/R \end{bmatrix} \quad (17e,f)$$

$$A_\omega = \begin{bmatrix} 0 & 0 & 0 \\ 0 & C & 0 \\ 0 & 0 & -C \end{bmatrix}, \quad P' = \begin{bmatrix} L & 0 & 0 \\ 0 & C & 0 \\ 0 & 0 & C \end{bmatrix} \quad (17g,h)$$

Equation (17a) clearly identifies the control parameters as the real variables $\langle d\rangle$, d'_{me}, ω, and v_g. Its steady-state vector, which is consistent with (10), can be used in the next linearized dynamic analysis.

4.3 The *o*ſ*b* Variational Equations

For this derivation, the control variables consist of ac small-signal perturbations, symbolized by careted lowercase, superimposed on dc quiescent values, symbolized by uppercase, i.e.,

$$\langle d\rangle = D + \hat{d}\ , \quad d'_{me} = D'_{me} + \hat{d}'_{me}$$

$$\omega = \Omega + \hat{\omega}, \quad \text{and} \quad v_g = V_g + \hat{v}_g \quad (18)$$

Naturally, the state vector also contains the corresponding constituents, i.e.,

$$\underline{x}' = \underline{X}' + \hat{\underline{x}}' \quad (19)$$

The linearized variational equation around a quiescent operating condition can now be attained by substitution of (18) and (19) into (17a) and neglect of second- and higher-order terms. Laplace transformation of both sides of the resulting equation then leads to the equivalent frequency-domain description

$$[sP'-(A_R+D'_{me}A_{d'}+j\Omega A_\omega)]\hat{\underline{x}}'(s) = A_{d'}\underline{X}'\hat{d}'_{me}(s) + A_\omega \underline{X}' j\hat{\omega}(s) + B_d V_g \hat{d}(s) + DB_d\hat{v}_g(s) \quad (20)$$

The phasor $\hat{v}_b$ or $\hat{v}_f$ as provided by (20) is not measurable owing to its complex nature. So its real part $\hat{v}_r$, imaginary part $\hat{v}_i$, or magnitude $\hat{v}_m$ needs to be defined in a state-to-output equation for measurement purposes. The state $\hat{i}$ can be used directly as an output because it is already real. The state-to-output relationship thus takes the form

$$\begin{bmatrix} \hat{i}(s) \\ \hat{v}_r(s) \\ \hat{v}_i(s) \\ \hat{v}_m(s) \end{bmatrix} = \begin{bmatrix} 1 & 0 & 0 \\ 0 & 1/2 & 1/2 \\ 0 & j/2 & -j/2 \\ 0 & V_b/2V_m & V_f/2V_m \end{bmatrix} \begin{bmatrix} \hat{i}(s) \\ \hat{v}_f(s) \\ \hat{v}_b(s) \end{bmatrix} \quad (21)$$

where

$$v_m^2(t) = v_f(t)\ v_b(t) \quad (22)$$

Equation (21) serves with (20) as the foundation for the ac small-signal analysis.

4.4 Poles of the Converter

Equations (20) and (21) represent a system of multiple outputs excited by multiple inputs. It is of interest to obtain the responses of the circuit when only one control is perturbed at a time, the others being constant. For example, if $\hat{\omega} = \hat{d} = \hat{v}_g = 0$, (20) reduces to

$$\left.\frac{\hat{\underline{x}}'(s)}{\hat{d}'_{me}(s)}\right|_{\substack{\hat{\omega}=\hat{d}=\\ \hat{v}_g=0}} = [sP'-(A_R+D'_{me}A_{d'}+j\Omega A_\omega)]^{-1}A_{d'}\underline{X}' \quad (23)$$

The remaining transfer functions from $\hat{\omega}$, $\hat{d}$, and $\hat{v}_g$ can be obtained in a similar fashion.

All dynamic responses turn out to share a common denominator:

$$K(s) = 1 + \left(RC + \frac{\Omega^2 LC^2 R}{2D'^2_{me}} + \frac{L}{2D'^2_{me}R}\right)s + \frac{LC}{D'^2_{me}}s^2 + \frac{LC^2R}{2D'^2_{me}}s^3 \quad (24)$$

born from the characteristic polynomial of $(A_R + D'_{me}A_{d'} + j\Omega A_\omega)$. It is reassuring that this equation emerges real amid all complex variable manipulations. This fact is a must as the original system is a realizable converter constructed from real L, C, and R. Owing to the nonlinear nature of the topology, the eigenvalues move as a function of the load as well as of the steady-state amplitude and frequency of the duty ratio modulation. A root locus for (24) is too cumbersome to be presented here; only results for the more practical case of low Ω will be discussed.

When the converter operates at a frequency sufficiently lower than the effective LC corner

$$\omega_o = \sqrt{2}\ \frac{D'_{me}}{\sqrt{LC}} \quad (25)$$

such that $(\Omega/\omega_o)^2 \ll 1$ and Ω can be dropped out of (24), the poles approximately satisfy

$$K(s) \simeq \left(1 + \frac{s}{\omega_p}\right)\left[1 + \frac{1}{Q}\frac{s}{\omega_o} + \left(\frac{s}{\omega_o}\right)^2\right] \quad (26a)$$

where

$$\omega_p = \frac{1}{RC} \quad \text{and} \quad Q = 2\frac{D'^2_{me}R}{\omega_o L} \quad (26b,c)$$

The complex corners resemble those of a flyback dc-to-dc converter: they are associated with the LC corner and directly proportional to the modulation amplitude D'_{me}. The real pole is just the RC combination encountered earlier in the steady-state formulas.

4.5 Zeros and Dc Gains of the Transfer Functions

The various control-to-output relations are obtained by combining (21) with (23) or other equations similar to (23). The poles of these responses have been analyzed in the preceding paragraphs, and some of their dc gains and zeros are tabulated in Table 1 below. This table actually features all the zeros that may occur in the outputs although it includes only five entries. Note that the results for $\hat{v}_g$ are not listed because they differ from those of $\hat{d}$ only in the dc gains.

Functions	DC Gains	Zeros
$\dfrac{\hat{v}_m}{\hat{d}'_{me}}\Big\vert_{\hat{v}_g=0}^{\hat{\omega}=\hat{d}=}$	$-\dfrac{DV_g}{2D'^2_{me}}\sqrt{1+\left(\dfrac{\Omega}{\omega_p}\right)^2}$	$\left(1-\dfrac{s}{\omega_z}\right)\left(1+\dfrac{s}{\omega_{z1}}\right)$
$\dfrac{\hat{i}}{\hat{\omega}}\Big\vert_{\hat{v}_g=0}^{\hat{d}'_{me}=\hat{d}=}$	$\dfrac{DV_g}{D'^2_{me}R}\dfrac{\Omega}{\omega_p^2}$	$1+\dfrac{s}{\omega_{z2}}$
$\dfrac{\hat{v}_i}{\hat{\omega}}\Big\vert_{\hat{v}_g=0}^{\hat{d}'_{me}=\hat{d}=}$	$-\dfrac{DV_g}{D'_{me}}\dfrac{1}{2\omega_p}$	$1+\dfrac{1}{Q_q}\dfrac{s}{\omega_o}+\left(\dfrac{s}{\omega_o}\right)^2$
$\dfrac{\hat{i}}{\hat{d}}\Big\vert_{\hat{v}_g=0}^{\hat{d}'_{me}=\hat{\omega}=}$	$\dfrac{V_g}{2D'^2_{me}R}\left[1+\left(\dfrac{\Omega}{\omega_p}\right)^2\right]$	$1+\dfrac{1}{Q_{z3}\omega_{z3}}\dfrac{s}{}+\left(\dfrac{s}{\omega_{z3}}\right)^2$
$\dfrac{\hat{v}_r}{\hat{d}}\Big\vert_{\hat{v}_g=0}^{\hat{d}'_{me}=\hat{\omega}=}$	$\dfrac{V_g}{2D'_{me}}$	$1+\dfrac{s}{\omega_p}$

where

$$\omega_o=\sqrt{2}\,\frac{D'_{me}}{\sqrt{LC}},\quad Q_q=\frac{2D'^2_{me}R}{\omega_o L[1-(\Omega/\omega_p)^2]}$$

$$\omega_p=\frac{1}{RC},\quad \omega_z=\frac{2D'^2_{me}R}{[1+(\Omega/\omega_p)^2]\,L},\quad \omega_{z1}=\left[1+\left(\frac{\Omega}{\omega_p}\right)^2\right]\omega_p$$

$$\omega_{z2}=2\omega_p,\quad \omega_{z3}=\sqrt{1+\left(\frac{\Omega}{\omega_p}\right)^2}\,\omega_p,\quad Q_{z3}=\frac{1}{2}\sqrt{1+\left(\frac{\Omega}{\omega_p}\right)^2}$$

Table 1. Dc gains and zeros of some transfer functions.

The first row of Table 1 displays $\hat{v}_m/\hat{d}'_{me}$ when other control inputs are held constant. Since $d'_{me} = d'_m/2\sqrt{3}$, $\hat{d}'_{me}$ implies *amplitude perturbation* of the sinusoidal duty ratio modulations. The response of $\hat{v}_m$ to this perturbation contains a rhp and a lhp zero, both moving around with D'_m and Ω. Not shown are $\hat{i}/\hat{d}'_{me}$ with lhp zeros at ω_{z1} and ω_{z2}, $\hat{v}_r/\hat{d}'_{me}$ with a lhp zero at ω_p and a rhp zero at ω_z, and $\hat{v}_i/\hat{d}'_{me}$ also with a rhp zero at ω_z.

The next two rows of Table 1 exhibit $\hat{i}/\hat{\omega}$ and $\hat{v}_i/\hat{\omega}$ when other perturbations are suppressed. Although it seems contrived to calculate the *frequency modulation* dynamics for a resistive load, the steps are useful when applied to, say, an induction motor load. Most interesting are the complex zeros in $\hat{v}_i/\hat{\omega}$ that stay nicely in the left half-plane when Ω is less than ω_p but then migrate into the right half-plane when Ω is greater than ω_p. Not included in Table 1 are $\hat{v}_r/\hat{\omega}$ with a zero at the origin and a lhp zero at $2\omega_p$ and $\hat{v}_m/\hat{\omega}$ with a rhp zero at ω_z.

The last two rows of Table 1 describe $\hat{i}/\hat{d}$ and $\hat{v}_r/\hat{d}$ when other control inputs are constant. The pair of lhp zeros in $\hat{i}$ give this transfer function the attractive single-pole characteristic. Not listed are $\hat{v}_m/\hat{d}$ with a lhp zero at ω_{z1} and $\hat{v}_i/\hat{d}$ without any zeros.

It is worth emphasizing that all results derived thus far, whether desirable or not, are for $\Phi_T = 0$, where Φ_T is the phase by which the *ofb* frame lags the duty ratio modulation of phase *a*, as given by (11d). In practice, letting Φ_T be zero is not always the best thing to do. *Judicious choice of* Φ_T can be proven to lead to *more favorable dynamics*. Even more encouraging are that results for $\Phi_T \neq 0$ can be constructed from those already computed for $\Phi_T = 0$ and that measurements for $\Phi_T \neq 0$ are just as convenient as those for $\Phi_T = 0$. These words will be verified experimentally in the next section.

5. EXPERIMENTAL VERIFICATION

5.1 Measurement Principle

The inductor current poses no measurement difficulty as it is dc and can be read directly using a current probe. Additional circuitry, however, must be added to "transform" the sinusoidal capacitor voltages to their equivalent dc descriptions. Straightforward implementation of the definitions

$$v_r\Big\vert_{\Phi_T} = \frac{1}{\sqrt{3}}\left[v_a\cos(\theta-\Phi_T) + v_b\cos(\theta-\Phi_T-120^0) + v_c\cos(\theta-\Phi_T+120^0)\right] \quad (27a)$$

$$v_i\Big\vert_{\Phi_T} = \frac{-1}{\sqrt{3}}\left[v_a\sin(\theta-\Phi_T) + v_b\sin(\theta-\Phi_T-120^0) + v_c\sin(\theta-\Phi_T+120^0)\right] \quad (27b)$$

and

$$v_m^2 = v_r^2 + v_i^2 \quad (27c)$$

obtainable from (11) is not very elegant as it requires excessive hardware. Fortunately, simple trigonometric manipulation of (11) suggests an alternative algorithm based on

$$v_r\Big\vert_{\Phi_{T2}} = v_r\Big\vert_{\Phi_{T1}}\cos(\Phi_{T2}-\Phi_{T1}) - v_i\Big\vert_{\Phi_{T1}}\sin(\Phi_{T2}-\Phi_{T1}) \quad (28a)$$

and

$$v_i\Big|_{\Phi_{T2}} = v_r\Big|_{\Phi_{T1}} \sin(\Phi_{T2}-\Phi_{T1}) + v_i\Big|_{\Phi_{T1}} \cos(\Phi_{T2}-\Phi_{T1}) \qquad (28b)$$

where Φ_{T1} and Φ_{T2} are any two arbitrary angles. Thus v_r and v_i, or any linear combination thereof, of one $o\!f\!b$ coordinate are always expressible as linear combinations of v_r and v_i of any other $o\!f\!b$ coordinate, the two coordinates differing in phase by an arbitrary constant amount. This important statement opens the gate to the dynamic analysis in rotating frames of non-zero phase lag touched upon at the end of Section 4. It also suggests that as long as Φ_T is allowed to vary, v_r *is all that is needed* to completely characterize the voltage phasor v_b. For example, if $\Phi_{T2} = 0$ and $\Phi_{T1} = 270^0$ in (28b),

$$v_i\Big|_{0^0} = v_r\Big|_{270^0} \qquad (29)$$

i.e., all transfer functions involving $\hat{v}_i$ derived for $\Phi_T = 0$ can be checked by reading $\hat{v}_r$ at $\Phi_T = 270^0$. Likewise, if Φ_T is set to Φ_v (Eq. (10b)), then

$$v_m = v_r\Big|_{\Phi_v} \qquad (30)$$

which represents an efficient way to verify the $\hat{v}_m$ frequency responses.

It is obvious that incorporation of a phase shifter in the measurement setup is beneficial. The following part will illustrate how this can be accomplished.

5.2 System Block Diagram

Figure 4 highlights the salient features of the signal processing circuits before and after the power stage. Observe that even though the actual inputs (v_g, d, and $d'_{i\alpha}$, where i = 1,2 and $\alpha \equiv$ a,b,c) and outputs (v_a, v_b, and v_c) of the converter itself may contain sinusoidally *time-varying* components, all inputs (v_g, <d>, <d'>, d'_m, and ω) and outputs (i, v_r, v_i, and v_m) on the periphery of the *overall system* are *purely dc* under steady-state condition. Thus the box labeled "Flyback Dc-to-Three-Phase Converter" belongs to the *abc* reference frame while the remaining blocks act like the "transformation" that converts the *abc* waveforms to the equivalent $o\!f\!b$ values.

The input section of Fig. 4 includes three PROM-D/A converter combinations to synthesize the balanced set of three-phase duty ratio modulations d'_a, d'_b, and d'_c (Eq. (7)). The reference input to the D/A converters, $d'_m/3$, controls the modulation amplitude. The analog input to the VCO, ω, governs the instantaneous modulation frequency. All ac ($<d'_{i\alpha}>$) and dc($<d'_{2\alpha}>$) duty ratios go through additional analog and digital signal processings before arriving at the power stage as drive waveforms.

The signal output section of Fig. 4 employs three D/A converters to multiply the three-phase outputs to three cosinusoidal functions. The products are then summed up to give either v_r (Eq. (27a)), v_i (Eq. (29)), or v_m (Eq. (30)), depending on the input to the phase shifter. The phase shifter is simply a binary adder inserted between the address buses of the input and output PROMs. Since the corresponding PROMs are programmed with identical sinusoids, their phase difference translates into the offset between their addresses. Note that the scheme used guarantees *the instantaneous speed of the $o\!f\!b$ coordinate equals the instantaneous inversion frequency* ω (Eq. (11d)).

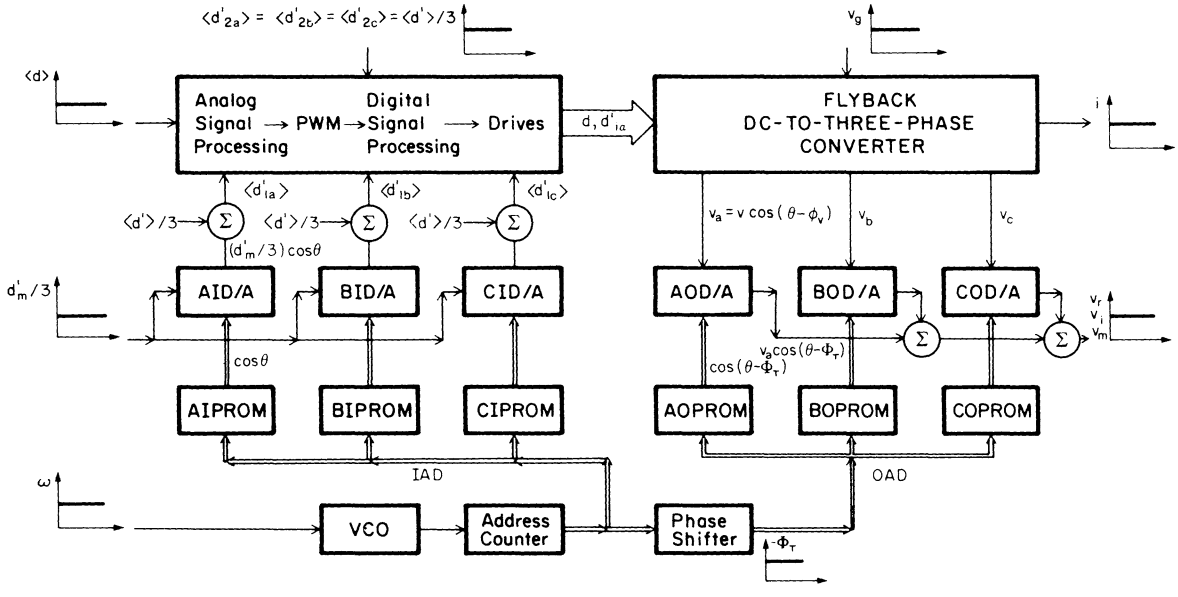

Fig. 4. System block diagram: the left half synthesizes duty ratios and switching functions; the right half transforms sinusoidal outputs into equivalent dc quantities.

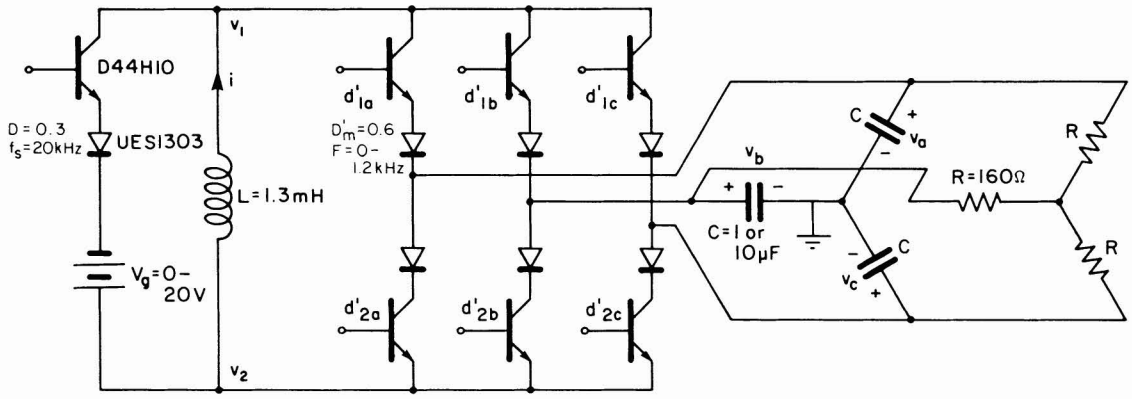

Fig. 5. Flyback dc-to-three-phase converter employing one energy transfer inductor, three output filter capacitors, and seven transistor/diode pairs to generate clean sinusoidal outputs.

5.3 Practical Implementation of the Power Stage

The realization of the flyback dc-to-three-phase converter of Fig. 2a centers around the two switches. Each switch has four different throws sequentially placed in series with the inductor, and since the inductor current is always dc, each throw has to carry only unidirectional current. The ac nature of the circuit then forces the off voltage across a throw to be the bipolar line-to-line voltage, as is obvious from Fig. 2a. This kind of two-quadrant-in-voltage throw can be implemented by cascading a transistor, which blocks the positive voltage, and a diode, which withstands the negative excursion, as illustrated with the rest of the circuit in Fig. 5. Note that more than two transistors in the whole structure can be simultaneously turned on without incurring any destruction.

A low power (10W) experimental unit was built to verify the steady-state and ac small-signal analyses. Formulas for steady-state current and voltages (Eq. (10)) guide the choice of semiconductor stresses. Fast switching devices with low on-drops and on-resistances are essential to minimize undesirable nonidealities. The following part will focus on the steady-state results.

5.4 Steady-State Waveforms

The oscillogram in Fig. 6 compares the three-phase outputs v_a, v_b, and v_c (second, third, and fourth trace, respectively) to the duty ratio modulation d'_a (first trace). Only close scrutiny reveals a slight amount of distortion in the lower three waveforms. *Absent* from the picture is the *cross-over distortion* commonly found in switched-mode amplifiers [5]. This type of distortion is due to the change in polarity of the finite switch drop when the switch current crosses zero. The flyback topology can circumvent this shortcoming because its switch current, being dc, never "crosses over" even though the output currents and voltages do. Note v_a lags d'_a by approximately 45^0 as predicted by (10b).

The data in Fig. 7 depict an overall drop of 60^0 in phase and an upward trend in the amplitude to confirm the "rhp zero" behavior in the steady-state capacitor voltages.

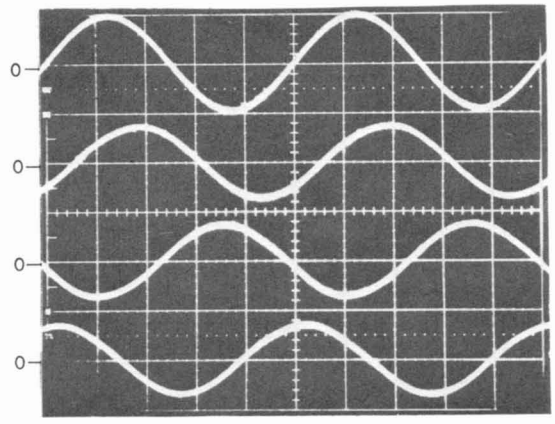

Fig. 6. v_a, v_b, and v_c (lower three traces) in contrast to d'_a (top trace) for V_g=15 V, F=100 Hz, and C=10 μF. Vertical scales: 2 V/div (top) and 20 V/div (lower three). Horizontal scale: 2 ms/div.

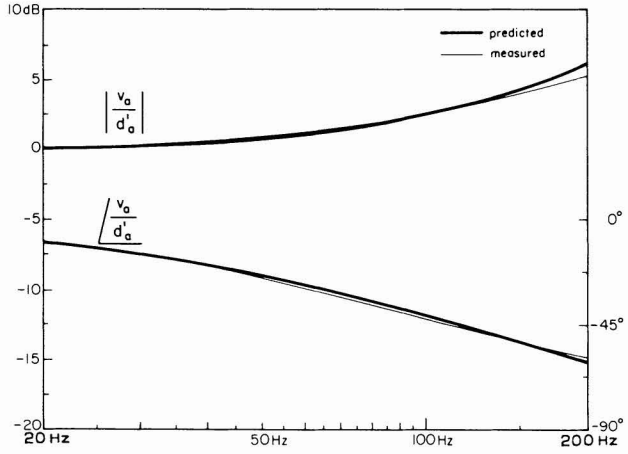

Fig. 7. Normalized amplitude and phase of v_a to confirm the "rhp" zero behavior. C=10 μF.

In Figs. 8 a fast sweep rate is used to look at the switching waveforms at the two ends of the inductor (Fig. 5). Each waveform has four intervals whose lengths indicate the duty ratios. The modulation edges are frozen at *zero frequency* in Fig. 8a to prove that the converter operates all the way down to dc. Observe in the last three intervals that the duty ratios, as well as the phase voltages, still constitute a set of *dc* three-phase values. As the frequency increases to 60 Hz in Fig. 8b, the four transition points within $D'T_s$ of v_1 trace out four beautiful ellipses to characterize simultaneous sinusoidal motions in both vertical, or voltage, and horizontal, or duty ratio, directions. The corresponding points in v_2 simply draw two vertical lines because $d'_{2\alpha}$ is dc. All useful information, such as D, D'_m, V, and Φ_v (Eq. (10b)), and a rough estimate of the waveform quality can be interpreted from Fig. 8b.

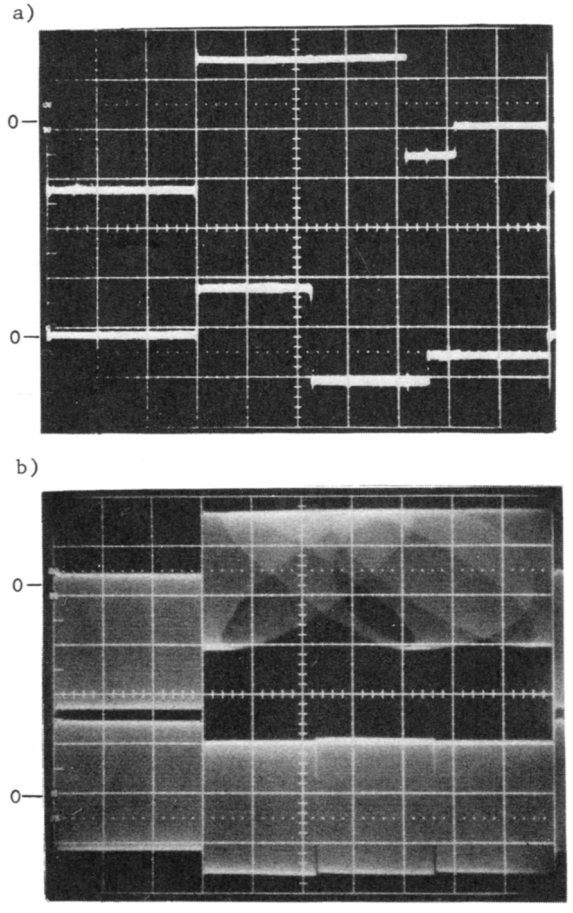

Fig. 8. v_1 (top trace) and v_2 (bottom trace) of Fig. 5 when V_g=15 V and C=10 μF for (a) F=0 Hz and (b) F=60 Hz. Vertical scale: 10 V/div. Horizontal scale: 5 μs/div.

5.5 Experimental Frequency Responses

Owing to the dc nature of all inputs and outputs, the well-known measurement techniques developed for dc-to-dc converters can be adapted to obtain the frequency responses of the new family of dc-to-three-phase converters. In this experiment the Automatic Measurement System [6] takes all the data and plots them in the familiar Bode format. The results are then overlaid on the theoretical curves predicted by the Switching Converter Analysis Program [6]. Proper modifications, however, have to be entered in the measurement program to condition it for noisy data. "Noise" used here refers to the harmonics that always exist owing to the finiteness of switching frequency, storage time modulation, and other component nonidealities. It dominates the small-signal responses, especially during fast high-frequency roll-off, although it is barely discernable at the power level of the test circuit adopted here.

Dynamic results are displayed in Figs. 9 through 12. Most prominent is the *wide bandwidth* of the circuit that leads to fast responses useful in applications such as motor drives. The captions beneath some plots indicate that the converter functions smoothly at as high as *1 kHz* (20 kHz is the switching frequency) where, apart from the ripples in the steady-state waveforms, all empirical data are still consistent with the state-space averaged predictions.

Figure 9 plots the amplitude-to-amplitude transfer function for C = 1 μF and F = 200 Hz. The circuit values place the real pole slightly below 1 kHz and the complex poles around 1.1 kHz. The net change of 270^0 in phase and the single-slope asymptote indicate the presence of both lhp and rhp zeros.

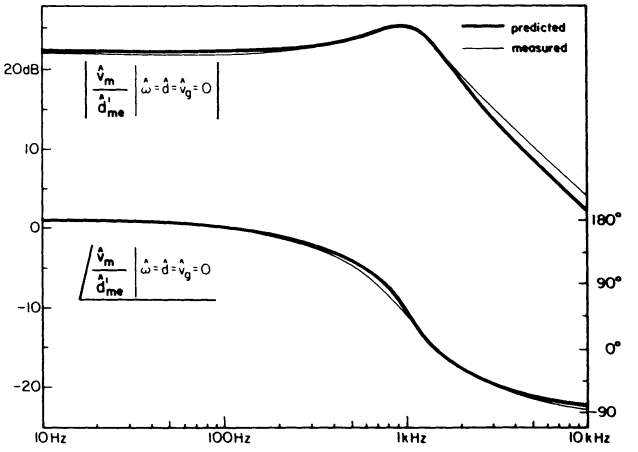

Fig. 9. $\hat{v}_m/\hat{d}'_{me}$ with lhp and rhp zeros at 1 kHz. C=1 μF, F=200 Hz, and V_g=15 V.

Figures 10 were devised to track the zeros in $\hat{v}_i/\hat{\omega}$ (Table 1). Again, C = 1 μF in order to place the RC corner at about 1 kHz, and measurements are made for F slightly below (Fig. 10a) and above (Fig. 10b) this corner. The similar amplitude plots in both figures confirm that the zeros are complex and have very high Q. The phase for F < 1 kHz, however, drops only 90^0 to indicate that the zeros are in the left half-plane while that for F > 1 kHz plunges down 450^0 to warn that they have migrated into the right half-plane!

a)

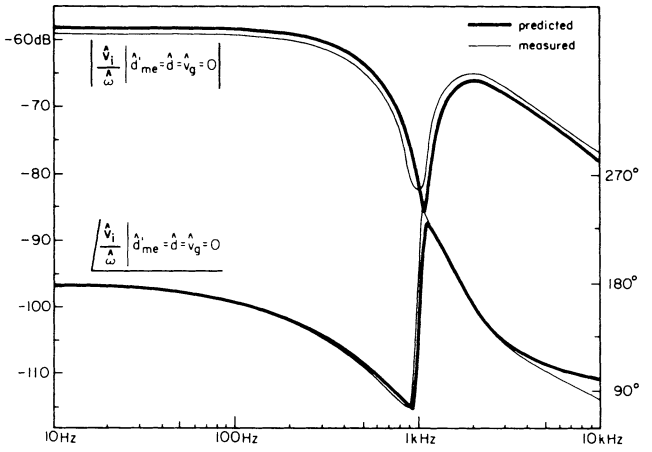

b)

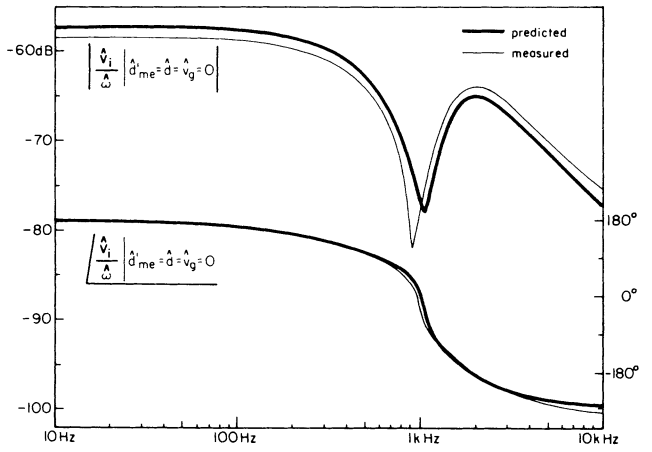

Fig. 10. $\hat{v}_i/\hat{\omega}$ with zeros in the lhp when F=900 Hz (a) moving into the rhp when F=1.1 kHz (b). f_p=1 kHz and V_g=14 V.

Among the "best" transfer functions is $\hat{i}/\hat{d}$ with a dominantly single-pole behavior (Table 1). Prediction and measurement both substantiate this fact in Fig. 11 for C = 10 μF. The zeros arrive at 220 Hz and dominate the earlier real pole at 70 Hz only to be overcome by the complex poles at 400 Hz.

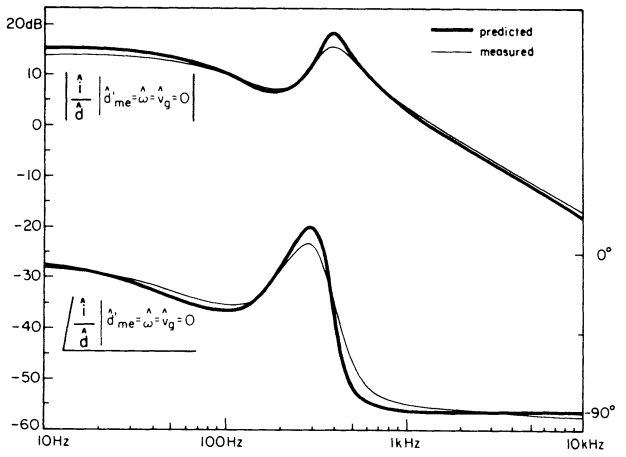

Fig. 11. $\hat{i}/\hat{d}$ with complex lhp zeros at 220 Hz. C=10 μF, F=200 Hz, and V_g=10 V.

All results reported up to this point were taken with Φ_T (Fig. 4) set at zero. Favorable dynamics, however, may exist in $o\!f\!b$ frames with proper non-zero Φ_T. This claim is verified for $\hat{v}_r/\hat{\omega}\big|_{-\Phi_T=55^0}$ in Fig. 12. Accentuating the graph are the sharp glitches owing to the complex lhp zeros. The ensuing single-slope roll-off is a reward for having selected the optimal frame of reference.

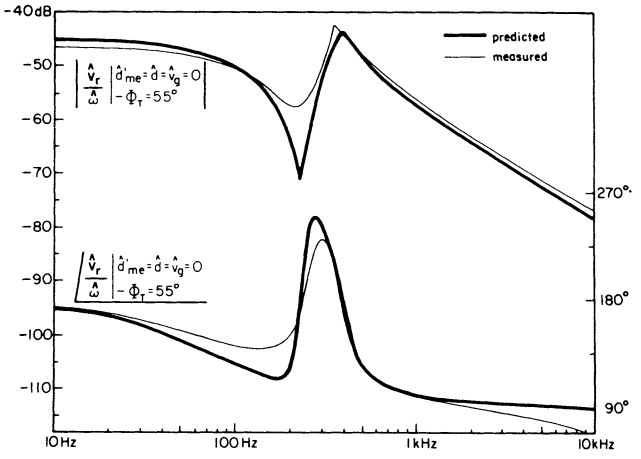

Fig. 12. Advantage of non-zero Φ_T: complex lhp zeros in $\hat{v}_r/\hat{\omega}$ at $-\Phi_T=55^0$. Same condition as in Fig. 11.

As has been demonstrated, theory and experiment agree remarkably well in describing steady-state as well as dynamic performances of the flyback dc-to-three-phase converter. The validity of state-space averaging assisted by the $o\!f\!b$ transformation is thus justified as a generalized, systematic analysis technique for the new class of dc-to-three-phase topologies.

6. CONCLUSION

A retrospective survey of the dc-to-ac inversion field has culminated in the discovery of a unified class of open-loop switching topologies that generate *sinusoidal polyphase outputs* from a dc input and easy-to-synthesize switching functions. As an example, a straightforward, logical algorithm is developed to synthesize the flyback dc-to-three-phase converter from its dc-to-dc counterpart. The resulting circuit, delineated in Fig. 5, retains the *single energy transfer inductor* and filters the switched current by three output capacitors. Two multiple-throw switches, realized by *seven* transistors and diodes, apply the inductor across the input and output voltages in the topology; their sinusoidal duty ratio modulations can have *independent* amplitudes and phases.

The new converter inverts power over a *broad frequency range*, starting from dc and approaching approximately a decade below the switching frequency. Steady-state analysis of the system in the stationary *abc* reference frame confirms *zero-averaged sinusoidal three-phase capacitor voltages* as well as *dc inductor current*. Dc inductor current, in turn, *prevents any cross-over distortion* in practical circuits. The steady-state voltage phasor exhibits an interesting *"rhp zero"* behavior to maintain volt-second balance across the inductor at higher inversion frequencies. Additional features include *isolation* and voltage step *up/down* capabilities.

Dynamic analysis is carried out in the rotating *αβb* coordinate system in which all steady-state outputs appear as real (inductor current) or complex (capacitor voltages) constants. In practical situations where the converter frequency is sufficiently low, the real pole coincides with the RC corner while the complex ones originate from an effective LC combination dependent on the modulation amplitude. The zeros in general vary with loading, modulation amplitude, and most pronouncedly, modulation frequency. They are found in both right and left halves of the s-plane. The *bandwidth* of the system is generally *wide* owing to fast switching frequency. Proper choice of phase for the *αβb* reference frame promises more optimal frequency responses.

Extension of this treatment to a motor load is straightforward: the conventional dynamic equations of the machine can be appended to the state-space averaged equations of the converter in a suitable reference frame. The smaller values of the reactive elements of the converter, as compared to those of the motor, usually simplify the analysis by decoupling the various modes of response.

The analysis techniques presented in this paper certainly apply to the buck, boost, etc., dc-to-three-phase converters as well. The topologies themselves can also be extended to other areas of energy conversion, the most trivial example being polyphase-to-dc rectification. The study of these generalized topics invites further discussion in the future.

REFERENCES

[1] Bimal K. Bose, "Adjustable Speed AC Drives — A Technology Status Review," Proc. of the IEEE, vol. 70, no. 2, pp. 116-135, February 1982.

[2] Farhad Barzegar and Slobodan Ćuk, "A New Switched-Mode Amplifier Produces Clean Three-Phase Power," Proc. Ninth International Solid-State Power Conversion Conference (Powercon 9), pp. E3.1-E3.15, July 1982.

[3] R. D. Middlebrook and Slobodan Ćuk, "A General Unified Approach to Modelling Switching Converter Power Stages," IEEE Power Electronics Specialists Conference, 1976 Record, pp. 18-34 (IEEE Publication 76CH1084-3 AES); also International J. of Electronics, vol. 42, no. 6, pp. 521-550, June 1977.

[4] Y. H. Ku, "Transient Analysis of Rotating Machines and Stationary Networks by Means of Rotating Reference Frames," Trans. AIEE, vol. 70, pt. I, pp. 943-957, 1951.

[5] Robert W. Erickson and R. D. Middlebrook, "Origins of Harmonic Distortion in Switching Amplifiers," Proc. Fourth Annual International PCI'82 Conference, pp. 567-582, March 1982.

[6] Farhad Barzegar, Slobodan Ćuk, and R. D. Middlebrook, "Using Small Computers to Model and Measure Magnitude and Phase of Regulator Transfer Functions and Loop Gain," Proc. Eighth International Solid-State Power Conversion Conference (Powercon 8), pp. H1.1-H1.28, April 1981.